Jet sharpening by turbulent mixing

D. G. Dritschel and R. K. Scott

References	**This article cites 17 articles, 1 of which can be accessed free** http://rsta.royalsocietypublishing.org/content/369/1937/754.full.html#ref-list-1
Rapid response	Respond to this article http://rsta.royalsocietypublishing.org/letters/submit/roypta;369/1937/754
Subject collections	Articles on similar topics can be found in the following collections atmospheric science (46 articles) applied mathematics (274 articles)
Email alerting service	Receive free email alerts when new articles cite this article - sign up in the box at the top right-hand corner of the article or click **here**

To subscribe to *Phil. Trans. R. Soc. A* go to:
http://rsta.royalsocietypublishing.org/subscriptions

Jet sharpening by turbulent mixing

By D. G. Dritschel* and R. K. Scott

School of Mathematics, University of St Andrews, Fife, UK

Jets or localized strong currents in planetary atmospheres, as well as in the Earth's oceans, are often associated with sharp potential-vorticity gradients owing to the inherent balance exhibited by these flows. Here, we explore and quantify jet sharpening in a simple idealized single-layer quasi-geostrophic model on a mid-latitude β-plane. The advantages of this idealization are that just two parameters control the flow development (the Rossby deformation length and the amplitude of the initial random flow perturbation), and that numerical experiments can comprehensively and accurately cover the parameter space. These experiments, carried out at unprecedented numerical resolution, reveal how an initially broad jet is sharpened, and the role played by coherent vortices in the vicinity of jets.

Keywords: jets; turbulent mixing; potential vorticity

1. Introduction

Large-scale zonal jets are observed in a wide range of geophysical flows, including those of the terrestrial atmosphere and oceans and, perhaps most strikingly, the atmospheres of the gas giant planets. They play a key role in the transport of heat, momentum and constituent tracers, including chemically and thermodynamically important quantities such as ozone and water vapour. Various dynamical processes have been considered with regard to their formation and maintenance against dissipation, including mixing due to Rossby-wave critical layers on the jet flanks [1], the arrest of the two-dimensional turbulent inverse energy cascade (e.g. [2–4], among many others) or the organization of small-scale eddy momentum fluxes by persistent latitudinal shear (e.g. [5]). Other authors have sought an explanation in terms of statistical–mechanical arguments (e.g. [6]).

These studies, and many others since (e.g. the special collection on Jets and Annular Structures in Geophysical Fluids; cf. [7,8]), have illuminated many aspects of jet formation and maintenance. However, the fact that jets are observed in such a wide range of dynamical regimes, and in the presence of very different forcing mechanisms, underlines the robustness of the dynamics involved, which is perhaps best understood in terms of the inhomogeneous mixing of potential vorticity (PV), comprising, in the simplest context, the relative vorticity and the vorticity owing to the planetary rotation. Zonal jets arise inevitably when PV

is mixed over limited latitudinal regions, regardless of the form of the mixing. This was discussed already by McIntyre [1] in the context of the winter polar stratosphere, where PV is mixed by Rossby wave breaking in the mid-latitude 'surf zone' bounded latitudinally by sharp gradients of PV. (A similar concept was recognized even earlier by Phillips [9] in the context of vertical mixing by internal wave breaking in stratified flows.) Mixing here means latitudinal mixing, across the planetary vorticity gradient, and acts to weaken local PV gradients in the mixing regions themselves, and strengthen them in between. Further, the non-local, long-range nature of the inversion operator relating the instantaneous PV field to the flow velocity gives rise to a dynamical resilience, whereby large latitudinal gradients of PV essentially inhibit large latitudinal displacements of material lines, thereby essentially suppressing mixing there. Regardless, therefore of the underlying cause of the mixing, whether by coherent eddies or by breaking of large-amplitude Rossby waves, the mixing of PV will be organized by the background flow into a highly inhomogeneous distribution. The zonal jets are a direct consequence of the resulting PV structure. For further discussion and references, see the recent reviews of Baldwin *et al.* [10] or McIntyre [11].

A limiting case can be considered in which the PV is perfectly mixed across adjacent regions, taking the form of a zonally symmetric staircase-like profile. The form of the jets arising in this situation was discussed in detail in Dritschel & McIntyre [7] and Dunkerton & Scott [8]. Both these studies showed a limiting relation, for the case of infinite Rossby deformation length, between jet strength and jet spacing, of the form $L_j = \sqrt{3}L_{Rh}$, where L_j is the distance between eastward jets, and L_{Rh} is the Rhines scale, $L_{Rh} = \sqrt{U_j/\beta}$, based on the peak eastward jet velocity U_j and planetary vorticity gradient β. The $\sqrt{3}$ factor is expected quite generally in any situation where the background angular momentum is quadratic in the appropriate latitudinal coordinate (y in the case of the β-plane, $\mu = \sin\phi$ on the sphere, where ϕ is latitude).

The analyses of Dritschel & McIntyre [7] and Dunkerton & Scott [8] considered the purely instantaneous structure of zonal jets. To understand their formation, or maintenance against dissipation, however, it is necessary to take into account the above eddy or wave mixing of PV in detail. At the simplest level, the Taylor identity relating eddy momentum flux convergence with the eddy flux of PV, reveals immediately how the formation of jets is connected to the eddy mixing of PV, and, in the context of two-dimensional flow, the acceleration of the jet core can be seen to be due directly to an upgradient flux of PV across the jet. Note, however, that upgradient here is in the sense of the traditional Eulerian zonal mean. Such upgradient fluxes are not inconsistent with the generalized mixing (advective mixing plus diffusion) considered in the study of Wood & McIntyre [12], which must be associated with purely downgradient fluxes at a local or molecular level. In other words, although local PV fluxes are downgradient, the large-scale flow can be such that fluxes may occur counter to the Eulerian zonal mean gradient. Thus, fig. 1*b,c* of Wood & McIntyre [12] is precluded not because of the presence of upgradient fluxes in the Eulerian zonal mean, but rather on account of the theorem proved later in that paper, which states that the net global angular-momentum change accompanying any physical mixing event must be negative.

Using a simple thought experiment, Wood & McIntyre [12] illustrate how mixing confined to the flanks of a pre-existing broad, weak jet results in the intensification of the PV gradients and zonal velocity in the jet core, while at the same time reducing the total angular momentum of the system. In that experiment, the jet is assumed to both start and end in a zonally symmetric state and only the final effect of the mixing on the flow is prescribed. This paper is motivated, in part, by the desire to examine how such a mixing may arise in a fully turbulent flow, and, in particular, how the presence of an initially broad, weak jet organizes the subsequent mixing preferentially on the jet flanks, leading to the positive feedback described above. This is done through a series of simple numerical experiments, described in §§2 and 3 below. To quantify the ensuing jet sharpening, we introduce (also in §3) a new diagnostic based on the topology of the full two-dimensional PV field. This diagnostic allows a clearer view of the intensification of PV gradients than both traditional Eulerian zonal averages or, surprisingly, equivalent latitude-based quantities; both of these work well in the limit of purely two-dimensional barotropic dynamics, when the final jets are nearly perfectly aligned zonally, but fail for different reasons when the Rossby deformation length becomes small.

2. Model and experimental design

(a) Equations of motion

We consider the quasi-geostrophic approximation to the rotating shallow water equations on the β-plane, where the Coriolis parameter $f = f_0 + \beta y$ is linear in y with constant gradient β. The equations reduce to the material advection of quasi-geostrophic PV, q,

$$q_t + J(\psi, q) = 0, \tag{2.1}$$

by a flow whose streamfunction ψ is related to q through

$$q = \beta y + \nabla^2 \psi - L_D^{-2} \psi, \tag{2.2}$$

where $L_D = \sqrt{gH}/f_0$ is the Rossby deformation length and where g is gravity and H is the mean layer depth. The case $L_D^{-1} \to 0$ corresponds to the case of purely two-dimensional, barotropic vortex dynamics. Equation (2.1) is solved in a doubly periodic domain of width 2π in both the x- and y-directions.

(b) Initial conditions

The initial conditions comprise a basic state PV $q_0(y)$, which is a function of y only, together with a spatially random perturbation $q'(x, y)$ of specified amplitude, which leads to turbulent mixing. The basic state follows that of Wood & McIntyre ([12], §10), and is given by

$$q_0(y) = \frac{2\pi\beta}{L_j\sqrt{\pi}} \int_0^y e^{-(y'/w)^2} \, dy', \tag{2.3}$$

where w is a measure of the width or smoothness of the jet. Note that for numerical convenience, we work in a doubly periodic domain of width $L = 2\pi$ and consider the case $\beta \neq 0$. This fixes the total change in q_0 across the domain
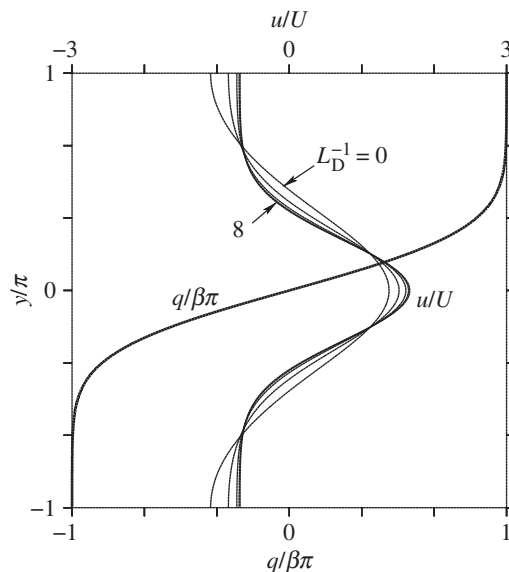
Figure 1. Initial basic state PV and velocity profiles, $q_0(y)$ and $u_0(y)$, the latter shown for values of $L_D^{-1} = 0, 2, 4, 6, 8$.

to be $2\pi\beta$. Equation (2.3) is adjusted by a multiplicative factor close to unity to ensure that $q_0 = \pm\beta L$ exactly at $y = \pm\pi$. In all the experiments below, we fix the width of the jet to be $w = 1$ and the background PV gradient to be $\beta = 2$. With these values, the form of q_0 is as shown in figure 1. We define a nominal unit of time as $T = 4\pi/(q_0(\pi) - q_0(-\pi))$, here equal to unity. The actual characteristic time depends on several factors (L_D^{-1}, amplitude of the perturbation q', etc.) in a complicated manner. We have ensured that all simulations were evolved long enough to reach a quasi-steady regime.

The basic state velocity profile, $u_0(y)$, then follows from equations (2.2) and (2.3). In an infinite domain, it is given by eqn (10.4) of Wood & McIntyre [12]. Here, there is a slight modification owing to the periodicity of the domain, but the profile is not substantially different. We further impose the condition that the y-averaged velocity is exactly zero. A number of profiles are shown in figure 1 for values of $L_D^{-1} = 0, 2, 4, 6, 8$. All profiles have been normalized by a velocity scale U that is obtained from u_0 weighted by the basic state PV gradient and integrating across the domain,

$$U = \frac{1}{2\pi\beta} \int_{-\pi}^{\pi} u_0 \frac{dq_0}{dy} \, dy. \tag{2.4}$$

This evaluates to $U = 2.57, 0.556, 0.172, 0.0801, 0.0459$ for the cases $L_D^{-1} = 0, 2, 4, 6, 8$, respectively.

The basic state PV is then perturbed by adding a random field q' whose energy spectrum takes the form $E(k) = ak^3 \exp[-2\pi(k/k_0)^2]$, where a and k_0 are constants. This has an enstrophy-energy centroid wavenumber at $k = k_0$ and peaks at wavenumber $\sqrt{3/4}k_0$. In all the calculations presented below, we use $k_0 = 16$, giving a perturbation whose scale is small relative to the initial jet width
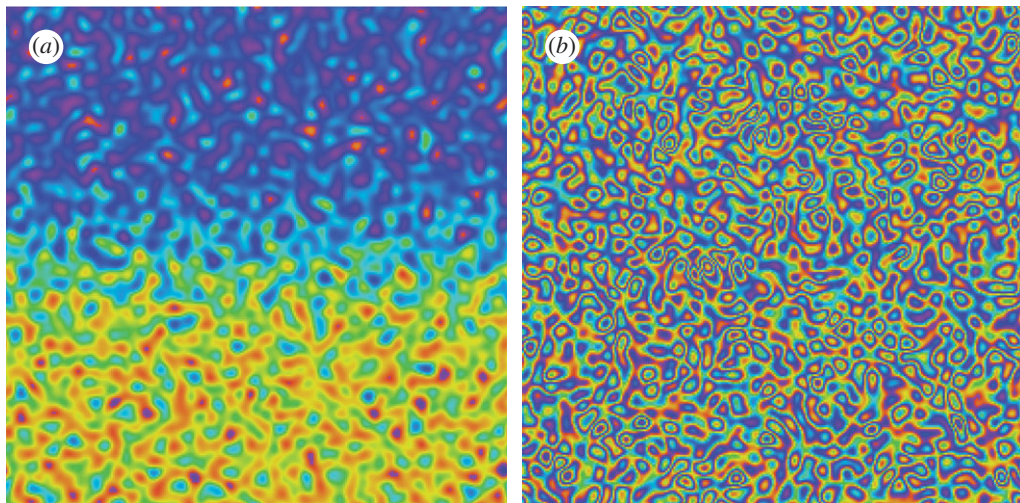
Figure 2. Initial PV field (basic state plus perturbation) for perturbation amplitudes (*a*) $q_e = 0.5$ and (*b*) $q_e = 4$. (Online version in colour. The colour range from red through to green/cyan to blue/purple represent values in the range $[-2\pi\beta, 2\pi\beta]$; outside this range, the colours are cycled periodically.)

and to the smallest deformation length considered. A suitable measure of the perturbation amplitude is defined as

$$q_e = \frac{q'_{\text{r.m.s.}}}{2\pi\beta}, \qquad (2.5)$$

the ratio of the r.m.s. perturbation to the PV contrast of the basic state across the domain. We consider the range of values $q_e = 0.5, 1, 2, 4$. The full PV fields (basic state plus perturbation) for the two cases $q_e = 0.5$ and $q_e = 4$ are shown in figure 2. Note that in the case $q_e = 4$, the perturbation field comprises values greatly exceeding those of the basic state, to the extent that the gradient of the basic state is not visible by eye. A list of the simulations performed is given in table 1.

(*c*) *Numerical algorithm*

The numerical simulations were carried out using a new, more accurate and flexible version of the contour-advective semi-Lagrangian (CASL) algorithm [13]. This new algorithm, called the combined Lagrangian advection method or 'CLAM' [14] is itself an extension of HyperCASL [15], which introduced a novel way of forcing flows and, furthermore, fixed all numerical-parameter dependencies. CLAM goes a step further than HyperCASL by computing the evolution of the total PV field q_s on a grid (here by the pseudo-spectral method) and blending this solution with that obtained by a set of PV contours, q_a, i.e. obtained by 'contour advection'. Essentially, a low-pass filter is applied to q_s and its complement is applied to q_a, thereby retaining the large-scale parts of q_s and the intermediate- to small-scale parts of q_a. This blending of solutions ensures that each method is used where it is most accurate, while not compromising

Table 1. List of the simulations performed together with the initial total energy $E = -\langle \psi q \rangle / 2$ and r.m.s. relative vorticity $\zeta_{\text{r.m.s.}}$.

L_{D}^{-1}	q_{e}	$E(0)$	$\zeta_{\text{r.m.s.}}(0)$
0	0.5	2.46581	2.69180
2	0.5	0.50585	1.46745
4	0.5	0.15324	1.33505
6	0.5	0.07443	1.56553
8	0.5	0.04323	1.28056
0	1	2.47818	3.75510
2	1	0.52251	3.11779
4	1	0.16332	2.60282
6	1	0.08695	2.87595
8	1	0.05702	2.68795
0	2	2.53923	6.91690
2	2	0.57795	6.13519
4	2	0.23228	6.37645
6	2	0.14140	5.76718
8	2	0.09578	4.84744
0	4	2.76178	12.47165
2	4	0.79742	12.12489
4	4	0.37946	10.48882
6	4	0.31457	10.56548
8	4	0.22126	8.74750

efficiency. An additional gridded residual field q_{d} is evolved to allow for forcing and to compensate for errors in contouring a smooth field by a discrete set of contours. At the beginning of every time step, q_{s} is initialized with the total PV field obtained at the end of the previous time step (combining q_{s}, q_{a} and q_{d}), and q_{d} is adjusted so that the total PV remains unchanged. Complete details and numerical tests are available in Dritschel & Fontane [14].

In the current work, a basic 'inversion' grid of 256×256 is used to compute the velocity field from the PV. For accuracy, the contour part q_{a} is obtained using a fast-fill routine on a grid four times finer in each direction, then averaged to the inversion grid [13]. On this grid, the quasi-geostrophic PV anomaly $q - \beta y$ is spectrally transformed using fast Fourier transforms, enabling a simple calculation of the velocity by wavenumber multiplication followed by inverse fast Fourier transforms. The PV is retained down to scales 16 times smaller, where it is dissipated by 'surgery', an efficient procedure that removes very thin filaments and joins very closely separated regions containing the same PV. This results in an exceptionally weak dissipation compared with other standard methods, as a recent comparison has demonstrated [16]. The other numerical parameters are functions of the grid resolution (see [15]). The only exception is the PV contour interval, here chosen to give 160 contour levels between the minimum and maximum initial PV. This is greater than the 40 recommended in Fontane & Dritschel [15] to better capture weak variations of PV in nearly homogenized regions of the flow at late times.
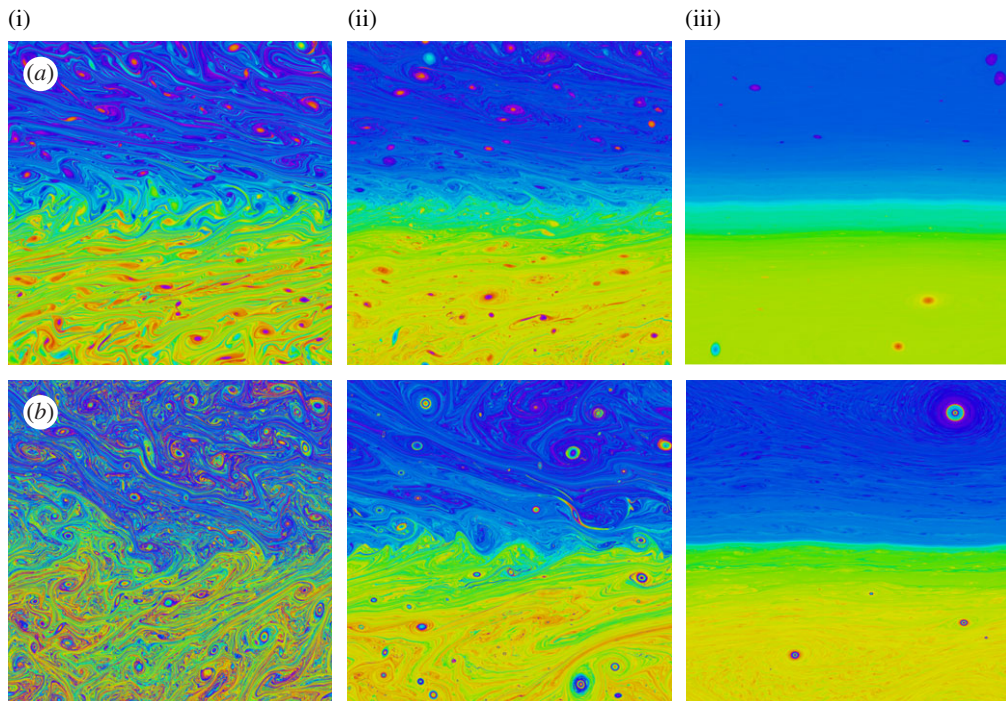
Figure 3. PV at times (i) $t = 5$, (ii) $t = 20$, (iii) $t = 200$ for the cases (a) $L_D^{-1} = 0$ and $q_e = 1$ and (b) $L_D^{-1} = 0$ and $q_e = 4$; colours as in figure 2. (Online version in colour.)

3. Results

(*a*) *General features of the evolution*

We consider first the case $L_D^{-1} = 0$ with a weak level of initial vorticity perturbation, $q_e = 1$. The behaviour is summarized in figure 3a, which shows snapshots of the PV at times $t = 5, 20, 200$ illustrating the main stages of the evolution. During the initial stage, up until around $t = 5$, the initial PV anomaly is strongly sheared by the velocity profile of the basic state jet. This gives way to an intermediate stage around $t = 20$, when most of the initial perturbation has been dissipated at small scales by the forward enstrophy cascade. At this point, a population of coherent vortices has emerged, which continues to mix PV in the region away from the jet. The vortices that persist in this stage are those that are sufficiently small and intense to survive the effects of the background shear. Notice that the central jet region, where the shear is weak, is largely free from coherent vortices, presumably a result of the well-known northward/southward drift of positive/negative vorticity anomalies on a background vorticity gradient (see [17] and references therein). The persistence of this effect in the presence of background jets was also noted recently [18]. Mixing of the PV during this stage occurs through a combination of the jet shear and the flow induced by the coherent vortices. By $t = 200$, a final, late stage has been reached, by which point almost all of the turbulent enstrophy has been dissipated, apart from a few
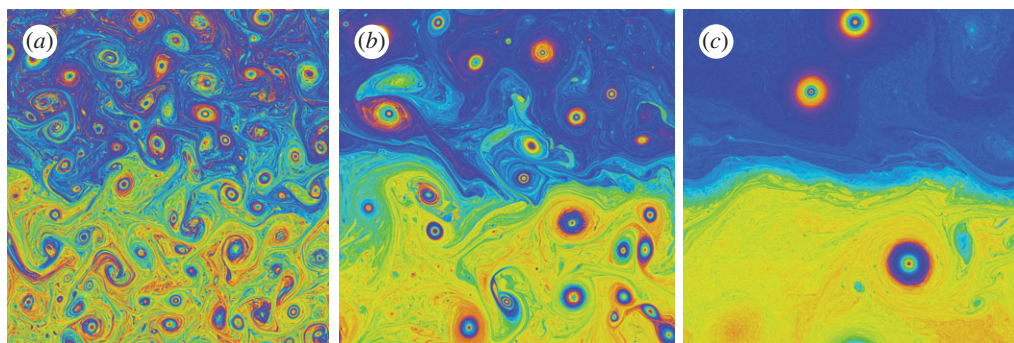
Figure 4. PV at times (*a*) $t = 10$, (*b*) $t = 40$, (*c*) $t = 400$ for the case $L_D^{-1} = 4$ and $q_e = 4$; colours as in figure 2. (Online version in colour.)

isolated vortices drifting in a region of almost zero background PV gradient. In contrast, the gradients in the central jet region have been enhanced, as will be quantified further below. Note that the final PV distribution is nearly zonally symmetric in this case.

Snapshots of the PV at the same times are shown in figure 3*b* for the case $L_D^{-1} = 0$ and $q_e = 4$. Although the initial perturbation is much stronger, and the initial shearing by the background flow is much more violent, the main characteristics of the evolution are broadly similar to the case with $q_e = 1$. In particular, the coherent vortices have again mostly left the central jet region by $t = 20$. In this case, the emergence of the central jet is clear at $t = 20$. Although still very undular as a result of the intense turbulent activity, by this time it nevertheless exhibits enhanced PV gradients across its core. These enhanced gradients are clear at $t = 200$, by which time the undulations on the jet have all but died out. Unsurprisingly, the vortices remaining at late times are more intense than for $q_e = 1$.

Finite, but large values of the Rossby deformation length, specifically $L_D^{-1} \lesssim 2$, introduce relatively minor changes to the evolution described above. The differences become greater at $L_D^{-1} = 4$ and above. At these values, the shorter range nature of the PV inversion operator means both that the shear associated with the basic state jet is weaker (see the values of U given at the end of §2) and that the vortices remain coherent on scales comparable to L_D. Further, the weaker basic state means that the ratio of perturbation PV to background shear is larger at larger L_D^{-1}, implying a more important role for coherent vortices in the mixing of background PV.

The evolution of the case $L_D^{-1} = 4$, $q_e = 4$ is shown in figure 4; later times are shown than for the $L_D^{-1} = 0$ cases reflecting the slower dynamics of the flow in this case. As predicted, there is less evidence of early and intermediate mixing by the background shear, but the flow is dominated by interactions of the strong coherent vortices. Additionally, these coherent vortices now exist all the way across the jet region (at $t = 20$ and $t = 40$). This is consistent with earlier studies of vortex drift on the β-plane, which showed slower drift at smaller L_D [17]. The vortices in the jet region induce strong meanders in the jet on the scale of the vortices. Again, because of the short-range nature of the PV inversion, these meanders persist at
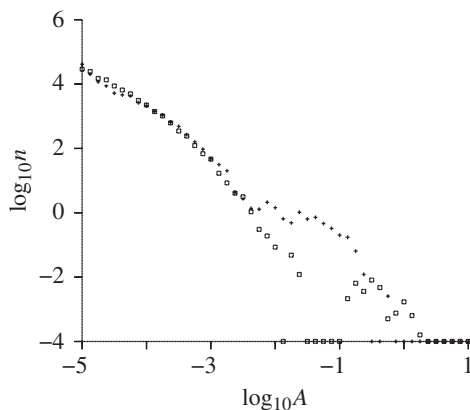
Figure 5. Vortex number density $n(A)$ versus area A averaged over two time periods $[10, 40]$ (plus symbols) and $[300, 400]$ (squares), for the case $L_D^{-1} = 4$ and $q_e = 4$ shown in figure 4. Vortices are defined to be contiguous regions (i) having a PV anomaly $|q - \beta y|$ above the global r.m.s. anomaly and (ii) having an eccentricity $2\lambda/(1 + \lambda^2) > 0.5$, where $\lambda \leq 1$ is the aspect ratio of an ellipse having the same area, first and second spatial moments. The cascade to larger scales is seen here by the emergence of vortices at the largest areas (square symbols on the right), and the related reduction of vortices at intermediate scales (by vortex merging).
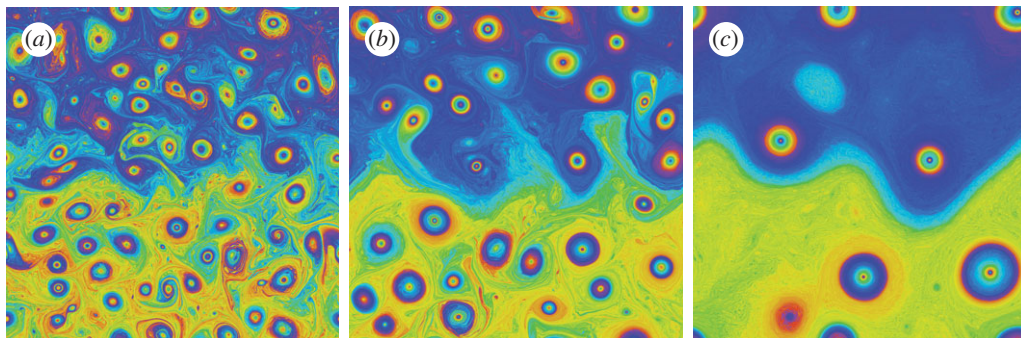

Figure 6. PV at times (*a*) $t = 25$, (*b*) $t = 100$, (*c*) $t = 1000$ for the case $L_D^{-1} = 8$ and $q_e = 4$; colours as in figure 2. (Online version in colour.)

late times ($t = 400$). Despite the meanders, however, a strong PV gradient is still apparent across the jet core, quantified in §3*b*. Finally, note that a clear inverse cascade is visible in the population of coherent vortices (figure 5), proceeding through successive vortex merger events and resulting only in three large vortices by $t = 400$.

The case of $L_D^{-1} = 8$, shown in figure 6, is similar to that of $L_D^{-1} = 4$, but yet more pronounced: the initial turbulent flow resulting from the perturbation completely dominates the effect of the jet shear. In this case, the final vortices induce strong meanders in the jet, with the whole pattern propagating to the left with relatively little change in form over time.
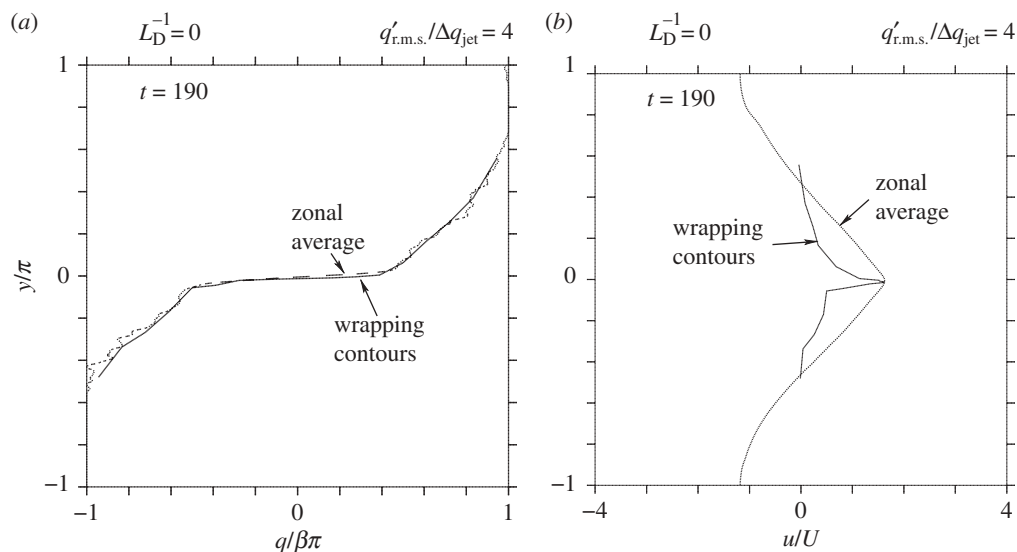
Figure 7. (*a*) Zonal mean PV as a function of y (dashed line) and PV as a function of y_e (solid line) and (*b*) zonal mean zonal velocity as a function of y and along-jet velocity as a function of y_e calculated according to equation (3.1). Both panels are at time $t = 190$ for the case $L_D^{-1} = 0$, $q_e = 4$.

(*b*) *Quantification of jet sharpening*

We next consider different measures of the mean PV gradient in the jet core. To illustrate the ideas most clearly, we focus here on the most extreme cases with $q_e = 4$; the results for smaller values of q_e are summarized in §3*c*.

The simplest way of averaging along the jet uses the traditional Eulerian zonal mean. In cases where the jet is zonally aligned with weak or no meanders (as in the cases of $L_D^{-1} = 0$ above), the zonal mean provides an accurate representation of the PV gradients across the jet and the corresponding along-jet velocity. These are shown in figure 7 (dashed lines) for the case $L_D^{-1} = 0$, $q_e = 4$. The PV gradients (figure 7*a*) in the jet core have increased significantly beyond their initial value (cf. figure 1), while those on the jet flanks have been effectively reduced to 0, giving rise to a clear PV 'staircase' as described above. The corresponding along-jet velocity (figure 7*b*) has increased in the jet core consistent with the enhanced PV gradients there. Note however that, in contrast to the thought experiment of Wood & McIntyre [12], the total angular momentum is invariant in this system.

Figure 8(*a,b*) shows the same zonal mean quantities (dashed lines) for the case $L_D^{-1} = 8$. Here, because of the strong jet meanders, the zonal average significantly underestimates the steep local PV gradients across the jet seen in figure 6, and the associated local along-jet velocities, effectively smearing out the jet. As the jet is aligned along the contours of constant PV, one improvement of the traditional Eulerian mean is to consider an average along these contours, an idea introduced originally by McIntyre [19]. In the usual way, we define the equivalent latitude y_e of a contour $\mathcal{C}$ of constant PV as the y-position of a straight, zonally aligned contour enclosing the same area as $\mathcal{C}$. This defines a monotonic function $y_e(q)$, which can be inverted to obtain PV as a function of y_e. Further, for a given q,
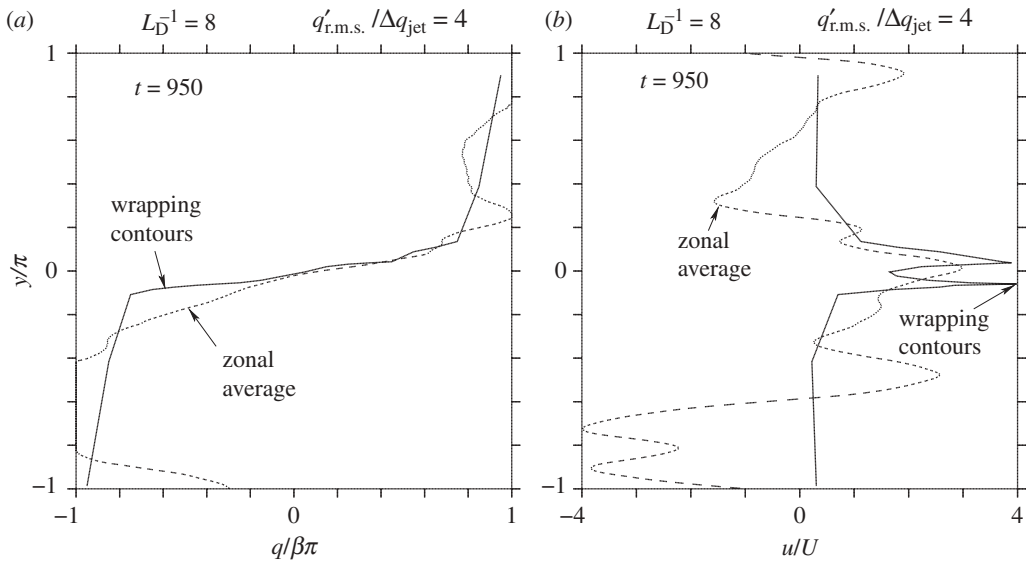
Figure 8. As in figure 7, but for the case $L_D^{-1} = 8$, $q_e = 4$ and at time $t = 950$.

we define an average along-contour velocity by an arc length weighted integral of the tangential component of $\mathbf{u}$ along $\mathcal{C}$,

$$u(q) = \frac{1}{L_{\mathcal{C}}} \int_{\mathcal{C}(q)} \mathbf{u} \cdot d\mathbf{x}, \qquad (3.1)$$

where $L_{\mathcal{C}} = \int_{\mathcal{C}(q)} ds$ is the arc length of $\mathcal{C}$. Together with $q(y_e)$, this gives an along-jet velocity as a function of y_e. The quantities $q(y_e)$ and $u(y_e)$ typically provide a better representation of jet gradients and velocities than the traditional zonal mean in cases when the jets exhibit strong departures from zonal symmetry. However, in cases when there are also large coherent vortices outside of the jet region, these vortices will contribute to the equivalent latitude in a way that does not necessarily reflect properties of the jet. Essentially, the area enclosed by a given PV contour located in the jet core may contain a contribution owing to PV values inside a strong cyclonic vortex to the south of the jet, or a strong anticyclonic vortex to the north, as may form from the pinching-off of a large jet meander. In regimes such as those considered here, where such vortices make up a significant fraction of the area within a contour, the standard equivalent latitude can give a highly distorted view of the jet.

A simple improvement is to consider, in the calculation of y_e, only those contours that wrap the domain in the x-direction. Restricting attention to such contours eliminates any contribution from closed vorticity regions away from the jet. An example is shown in figure 9, taken from the case $L_D^{-1} = 8$, $q_e = 4$ at $t = 1000$. Only the contours that wrap the domain are plotted. Most of these lie within the jet region, and the voids associated with coherent vortices on the flanks are evident. Note that the initial distribution of PV contours is determined by equation (2.3); the contours are equally spaced in q and so weakly concentrated near $y = 0$ by the error-function profile. By $t = 1000$, the effect of the turbulent mixing is such as to bunch the contours more tightly around $y = 0$.
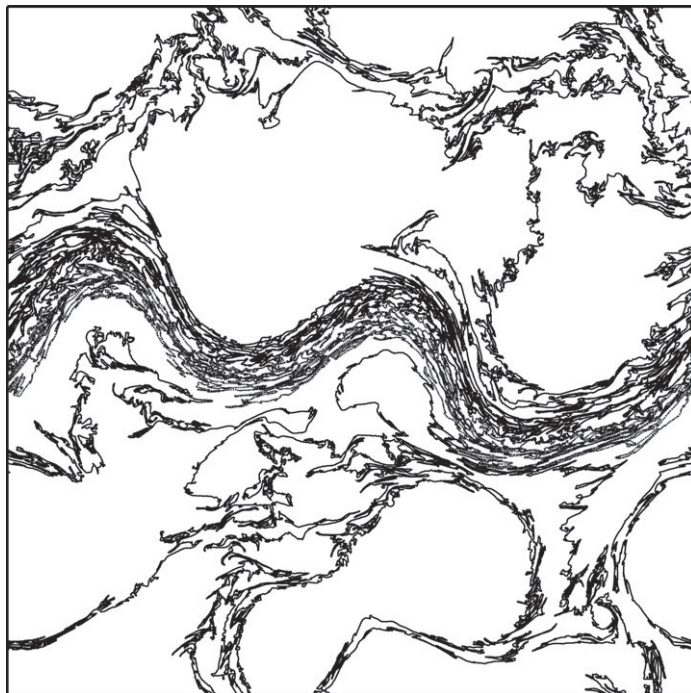
Figure 9. Wrapping contours in the case $L_D^{-1} = 8$, $q_e = 4$ at $t = 1000$.

The quantities $q(y_e)$ and $u(y_e)$ as a function of equivalent latitude y_e, thus restricted to wrapping contours, are shown for the above cases by the solid lines in figures 7 and 8. For the case $L_D^{-1} = 0$, the equivalent latitude quantities agree closely with the traditional zonal means for the reasons just stated ($u(y_e)$ is more peaked because of the increase in contour lengths L_C from filamentation away from the jet core). For the case $L_D^{-1} = 8$, however, figure 7 shows a markedly different structure in the jet core. In the PV $q(y_e)$, two distinct regions of very steep gradients are visible, which are missed altogether by the zonal mean. This structure is also visible in the along-jet velocity profile $u(y_e)$, which shows a clear double-peak structure, again not captured by the zonal mean.

The emergence in time of the fine-scale structure is shown in figure 10. Note that the early values of $u(y_e)$ are generally larger than those of the basic state, on account of the initial PV perturbation, and because the jet is very weak at this time. Nevertheless, the fine-scale structure begins to appear already at $t = 50$ in both $q(y_e)$ and $u(y_e)$. It is well established by $t = 250$ and strengthens only slightly thereafter.

The persistence of the double jet between $t = 250$ and $t = 1000$ is of interest in itself. Despite the proximity of the jets, they show no sign of merging into a single stronger jet. In fact, in this and many other model integrations, including integrations of forced-dissipative turbulence, it was found that two nearby jets may coexist for a surprisingly long time, much longer than the time taken to reach a statistical equilibrium.
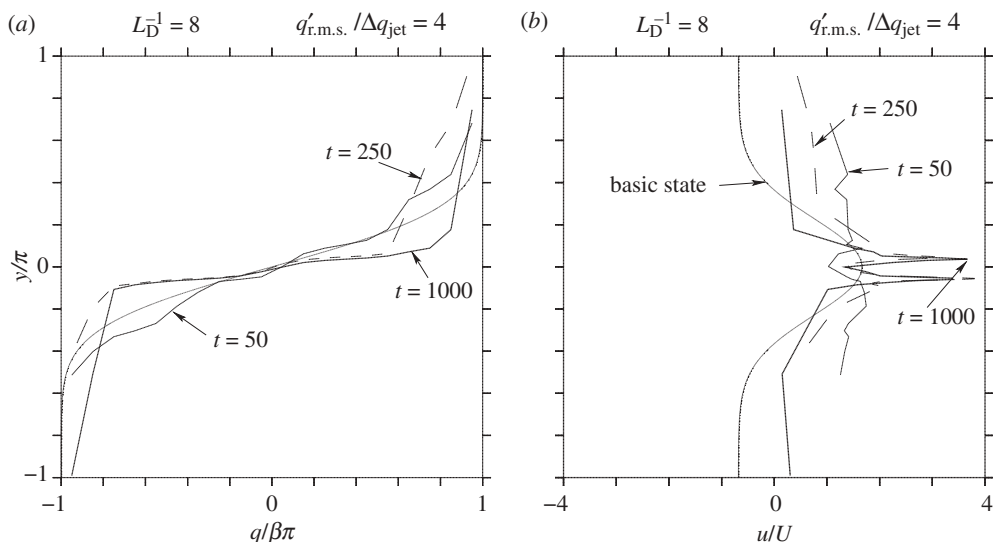
Figure 10. Evolution of (*a*) $q(y_e)$ and (*b*) $u(y_e)$ for the case $L_D^{-1} = 8$, $q_e = 4$.

(*c*) *Summary across all parameters*

Finally, to summarize the degree of jet sharpening across the full range of parameter values, we consider two integral measures of the PV gradient and along-jet speed. To focus attention on the relevant quantities in the vicinity of the jet core, we define a jet-weighted average by multiplying the quantity of interest by the appropriate mean PV gradient before integrating across the domain. For a zonal mean function $\bar{f}(y)$, we define the jet-weighted average simply as

$$\langle \bar{f} \rangle = \frac{1}{Q} \int_{-\pi}^{\pi} \bar{f}(y) \frac{\mathrm{d}\bar{q}}{\mathrm{d}y} \, \mathrm{d}y, \tag{3.2}$$

where $Q = \int_{-\pi}^{\pi} (\mathrm{d}\bar{q}/\mathrm{d}y) \, \mathrm{d}y = 2\pi\beta$ is the PV contrast across the channel. When $\bar{f} = \mathrm{d}\bar{q}/\mathrm{d}y$, the PV gradient, this is just the ratio of the L_2 and L_1 norms of $\mathrm{d}\bar{q}/\mathrm{d}y$.

On the other hand, when f is a given function of PV q or equivalent latitude, y_e, we define

$$\langle f \rangle = \frac{1}{Q} \int_{q(-\pi)}^{q(\pi)} f(q) \, \mathrm{d}q = \frac{1}{Q} \int_{-\pi}^{\pi} f(y_e) \frac{\mathrm{d}q}{\mathrm{d}y_e} \, \mathrm{d}y_e, \tag{3.3}$$

in which q is written as a function of y_e (this is possible because the inverse function $y_e(q)$ is monotonic). Again, the normalization $Q = \int_{-\pi}^{\pi} (\mathrm{d}q/\mathrm{d}y_e) \, \mathrm{d}y_e = 2\pi\beta$. As discussed above, in the calculation of y_e, we only consider PV contours that wrap the domain in the x-direction.

Figure 11 shows both averages, based on equivalent latitude and zonal mean, for the case $f = \mathrm{d}q/\mathrm{d}y_e$ and $\bar{f} = \mathrm{d}\bar{q}/\mathrm{d}y$. In each case, the values are normalized by the basic state value (which is the same for both diagnostics, but varies with L_D^{-1}). Both quantities show a general increase of the across-jet PV gradient with
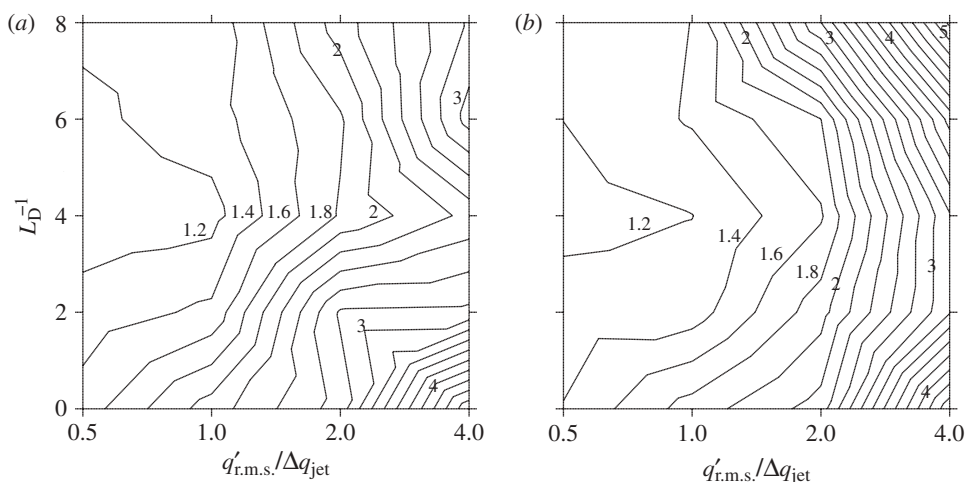
Figure 11. Jet-weighted averages of PV gradient for all calculations $q_e = 0.5, 1, 2, 4$ and $L_D^{-1} = 0, 2, 4, 6, 8$: (*a*) based on equivalent latitude $\langle dq/dy_e \rangle$ and (*b*) based on the zonal mean $\langle d\bar{q}/dy \rangle$. Values are normalized by the value of the corresponding basic state.
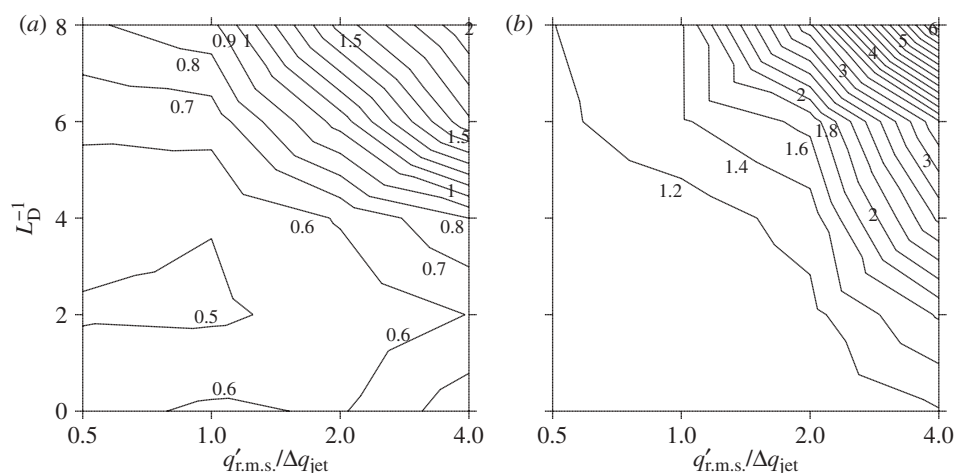

Figure 12. Jet-weighted averages of along-jet velocity for all calculations $q_e = 0.5, 1, 2, 4$ and $L_D^{-1} = 0, 2, 4, 6, 8$: (*a*) based on equivalent latitude $\langle u(y_e) \rangle$ and (*b*) based on the zonal mean $\langle \bar{u} \rangle$. Values are normalized by the value of the corresponding basic state.

increasing turbulent intensity q_e, as expected. Surprisingly, the zonal mean shows a stronger intensification of the across-jet gradients, particularly at large L_D^{-1}. This is because there are large contributions to the zonal-mean PV gradient well away from the jet core—as seen for example in figure 8*a*. These contributions are associated with the coherent vortices seen in figure 6. Hence, the zonal mean PV gradient does not directly quantify the jet. The equivalent latitude mean, on the other hand, provides a true measure of the PV gradient intensification of the jet.

The jet-weighted averages with $f = u(y_e)$ and $\bar{f} = \bar{u}$ are shown in figure 12. Both quantities again show an increase with q_e and now also with L_D^{-1}. The increase with L_D^{-1} is due, in part, to the decrease of the corresponding values of the basic state. Again, the zonal mean averages are, in general, significantly larger than averages based on equivalent latitude. Once again, this difference is because of contributions from coherent vortices in the zonal mean. The zonal mean is strikingly different from the equivalent latitude mean particularly at large L_D^{-1}, as illustrated in figure 8*b* for $L_D^{-1} = 8$. Only the equivalent latitude mean directly measures jet sharpening. Strongest jet intensification occurs for large q_e and L_D^{-1}, although some intensification also occurs at smaller L_D.

4. Conclusions

By way of a set of simple numerical experiments, we have addressed the nature of jet emergence from a fully turbulent flow. The numerical method used here takes advantage of recent extensions to the well-tested CASL method, and combines the efficiency of contour dynamics at representing small-scale structures, with the robustness of the pseudo-spectral method at conserving large-scale quantities such as energy and momentum. The new combined method permits an unprecedentedly detailed examination of freely decaying β-plane turbulence, which requires a near dissipation-less representation of the evolution, on account of the long integration times needed to reach equilibrium, as well as robust conservation properties.

A key finding in this study is that jet emergence from a turbulent flow occurs in two main stages. The first, early stage is characterized by the mixing of PV anomalies by the basic state shear associated with the weak initial jet. This is followed by a second, longer stage in which the mixing is enhanced by coherent vortices that emerge in an inverse energy cascade from the small-scale initial perturbation. In each stage, the mixing is confined to the jet flanks: in the first stage because the shear has a minimum in the jet core, and in the second stage because the coherent vortices tend to drift away from the jet core on the background PV gradient. The relative importance of the two stages depends on the initial ratio of perturbation vorticity to basic state shear.

In quantifying jet intensification, the traditional Eulerian zonal mean may significantly underestimate the across-jet PV gradient and along-jet velocity, particularly in cases when the Rossby deformation length is small and the jet is highly undular. Diagnostics based on equivalent latitude provide a better picture in these cases, but even here can be obscured by contributions from large coherent vortices that are not part of the jet itself. This limitation was overcome in this study by imposing a topological constraint, namely considering only those PV contours that wrap the domain zonally in the calculation of equivalent latitude.

Over the wide range of cases examined, from weak to strong levels of turbulence q_e, and from small to large Rossby deformation lengths L_D, the mixing of PV was found to steepen PV gradients across the jet core and reduce them on the flanks. This restructuring of the PV field, however, does not always result in a strong intensification of the along-jet velocity. Strong intensification is mainly found for large values of q_e.

Perhaps, the most striking feature of the above calculations is the degree of influence of the initial jet when the initial perturbation is strong, $q_e = 4$. In the initial PV field, shown in figure 2b, the gradient of the basic state is completely dominated by the perturbation. That this field evolves robustly to the states shown in figures 3–6 (right), comprising a sharp jet located exactly at $y = 0$, is truly remarkable. An alternative view would be to consider the perturbation field q' as a prescribed initial isotropic 'basic state' and to consider the jet q_0 as a zonal 'perturbation'; then our results show that a relatively small zonal perturbation is sufficient to nudge the evolution into a given configuration. In other words, a slight strengthening of the initial PV gradients in the centre of the domain results in the emergence of a jet at precisely that location. This provides a clear illustration of the robustness of the positive feedback effect described in the introduction, whereby a small perturbation to the zonal mean PV gradient will amplify owing to its organization of the turbulent eddy mixing.

References

1 McIntyre, M. E. 1982 How well do we understand the dynamics of stratospheric warmings? *J. Meteorol. Soc. Jpn.* **60**, 37–65. (Special issue in commemoration of the centennial of the Meteorological Society of Japan (ed. K. Ninomiya)).

2 Rhines, P. B. 1975 Waves and turbulence on a β-plane. *J. Fluid Mech.* **69**, 417–443. (doi:10.1017/S0022112075001504)

3 Salmon, R. 1982 Geostrophic turbulence. In *Topics in ocean physics* (eds A. R. Osbourne & P. Malanotte Rizzoli). Proceedings of the International School of Physics Enrico Fermi (July 1980), Course LXXX.

4 Maltrud, M. E. & Vallis, G. K. 1991 Energy spectra and coherent structures in forced two-dimensional and beta-plane turbulence. *J. Fluid Mech.* **228**, 321–342. (doi:10.1017/S0022112091002720)

5 Huang, H.-P. & Robinson, W. A. 1998 Two-dimensional turbulence and persistent zonal jets in a global barotropic model. *J. Atmos. Sci.* **55**, 611–632. (doi:10.1175/1520-0469(1998)055<0611:TDTAPZ>2.0.CO;2)

6 Bouchet, F. & Sommeria, J. 2002 Emergence of intense jets and Jupiter's Great Red Spot as maximum entropy structures. *J. Fluid Mech.* **464**, 165–207. (doi:10.1017/S0022112002008789)

7 Dritschel, D. G. & McIntyre, M. E. 2008 Multiple jets as PV staircases: the Phillips effect and the resilience of eddy-transport barriers. *J. Atmos. Sci.* **65**, 855–874. (doi:10.1175/2007JAS2227.1)

8 Dunkerton, T. J. & Scott, R. K. 2008 A barotropic model of the angular momentum conserving potential vorticity staircase in spherical geometry. *J. Atmos. Sci.* **65**, 1105–1136. (doi:10.1175/2007JAS2223.1)

9 Phillips, O. M. 1972 Turbulence in a strongly stratified fluid—is it unstable? *Deep Sea Res.* **19**, 79–81. (doi:10.1016/0011-7471(72)90074-5)

10 Baldwin, M. P., Rhines, P. B., Huang, H.-P. & McIntyre, M. E. 2007 The jet-stream conundrum. *Science* **315**, 467–468. (doi:10.1126/science.1131375)

11 McIntyre, M. E. 2008 Potential-vorticity inversion and the wave-turbulence jigsaw: some recent clarifications. *Adv. Geosci.* **15**, 47–56. (doi:10.5194/adgeo-15-47-2008)

12 Wood, R. B. & McIntyre, M. E. 2010 A general theorem on angular-momentum changes due to potential vorticity mixing and on potential-energy changes due to buoyancy mixing. *J. Atmos. Sci.* **67**, 1261–1274. (doi:10.1175/2009JAS3293.1)

13 Dritschel, D. G. & Ambaum, M. H. P. 1997 A contour-advective semi-Lagrangian numerical algorithm for simulating fine-scale conservative dynamical fields. *Quart. J. Roy. Meteorol. Soc.* **123**, 1097–1130. (doi:10.1002/qj.49712354015)

14 Dritschel, D. G. & Fontane, J. 2010 The combined Lagrangian advection method. *J. Comput. Phys.* **229**, 5408–5417. (doi:10.1016/j.jcp.2010.03.048)

15 Fontane, J. & Dritschel, D. G. 2009 The HyperCASL algorithm: a new approach to the numerical simulation of geophysical flows. *J. Comput. Phys.* **228**, 6411–6425. (doi:10.1016/j.jcp.2009.05.025)

16 Dritschel, D. G. & Scott, R. K. 2009 On the simulation of nearly inviscid two-dimensional turbulence. *J. Comp. Phys.* **228**, 2707–2711. (doi:10.1016/j.jcp.2009.01.015)

17 Lam, J. S.-L. & Dritschel, D. G. 2001 On the beta-drift of an initially circular vortex patch. *J. Fluid Mech.* **436**, 107–129. (doi:10.1017/S0022112001003974)

18 Scott, R. K. In press. Polar accumulation of cyclonic vorticity. *Geophys. Astrophs. Fluid Dyn.*

19 McIntyre, M. E. 1980 Towards a Lagrangian mean description of stratospheric circulations and chemical transport. *Phil. Trans. R. Soc. Lond. A* **296**, 129–148. (doi:10.1098/rsta.1980.0160)